ACS NANO
Cite This: ACS Nano 2019, 13, 14241−14251
www.acsnano.org

ARTICLE

Dendrimer Ligand Directed Nanoplate Assembly

Katherine C. Elbert,[†,#] Thi Vo,[‡,#] Nadia M. Krook,[§] William Zygmunt,[‡] Jungmi Park,[†] Kevin G. Yager,[∥] Russell J. Composto,[§] Sharon C. Glotzer,[*,‡,⊥,¶] and Christopher B. Murray[*,†,§]

[†]Department of Chemistry, University of Pennsylvania, Philadelphia, Pennsylvania 19104, United States
[‡]Department of Chemical Engineering, University of Michigan, Ann Arbor, Michigan 48109, United States
[§]Department of Materials Science and Engineering, University of Pennsylvania, Philadelphia, Pennsylvania 19104, United States
[∥]Center for Functional Nanomaterials, Brookhaven National Laboratory, Upton, New York 11973, United States
[⊥]Department of Materials Science and Engineering, University of Michigan, Ann Arbor, Michigan 48109, United States
[¶]Biointerfaces Institute, University of Michigan, Ann Arbor, Michigan 48109, United States

Supporting Information

ABSTRACT: **Many studies on nanocrystal (NC) self-assembly into ordered superlattices have focused mainly on attractive forces between the NCs, whereas the role of organic ligands on anisotropic NCs is only in its infancy. Herein, we report the use of a series of dendrimer ligands to direct the assembly of nanoplates into 2D and 3D geometries. It was found that the dendrimer-nanoplates consistently form a directionally offset architecture in 3D films. We present a theory to predict ligand surface distribution and Monte Carlo simulation results that characterize the ligand shell around the nanoplates. Bulky dendrimer ligands create a nontrivial corona around the plates that changes with ligand architecture. When this organic−inorganic effective shape is used in conjunction with thermodynamic perturbation theory to predict both lattice morphology and equilibrium relative orientations between NCs, a lock-and-key type of mechanism is found for the 3D assembly. We observe excellent agreement between our experimental results and theoretical model for 2D and 3D geometries, including the percent of offset between the layers of NCs. Such level of theoretical understanding and modeling will help guide future design frameworks to achieve targeted assemblies of NCs.**

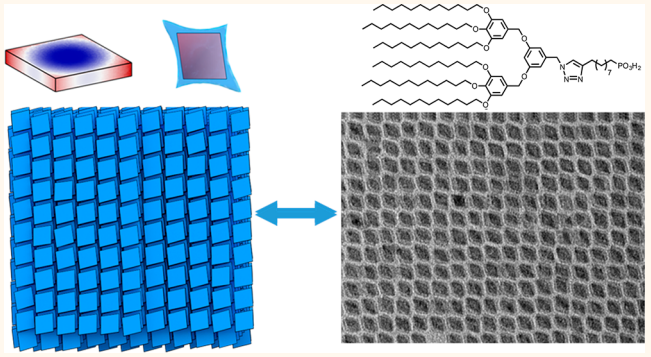

KEYWORDS: *nanocrystal, nanoplate, self-assembly, dendrimer, lattice prediction, polymer scaling, perturbation theory*

Anisotropic nanocrystals (NCs) have been employed to create a wide variety of assembled superlattices, giving access to novel properties of the resulting films.[1−3] Control and uniformity of film architecture is of the upmost importance for NC technology; however, there is still much to be understood about the formation of these assemblies. Contributing factors during assembly include NC−NC interactions,[4−6] NC shape,[7,8] ligand effects,[9−11] and fabrication method, which encompasses a variety of variables such as subphase polarity,[12,13] drying rate,[14] and electric fields.[15,16] Although many of these factors have been investigated previously, typically, these studies utilize commercially available organic ligands, whereas few examples exist for intentionally designed combinations,[17−19] particularly for anisotropic NCs. It is well-known that self-assemblies of NCs rely on both organic and inorganic components of the NC building blocks;[20] however, ligand design and direct comparisons to elucidate ligand effects on NC assemblies still remain a rich area for research into diverse superlattices.

Ligand effects on NC assembly can be emphasized by employing anisotropic NCs, as differences between ligand grafting densities on various facets of the NCs can have a large effect on the resulting assembly.[18,21,22] Previous work has shown that longer ligands of DNA preferentially bind to different faces of NC cubes due to ligand−ligand interactions on the surfaces of the NCs.[23] Simulation and theoretical approaches aimed at characterizing the degree of ligand partitioning as a function of faceting and relative curvature have revealed a critical interplay between ligands and the core geometry that results in the formation of nontrivial ligand

Received: September 17, 2019
Accepted: November 22, 2019
Published: November 22, 2019

DOI: 10.1021/acsnano.9b07348
ACS Nano 2019, 13, 14241−14251

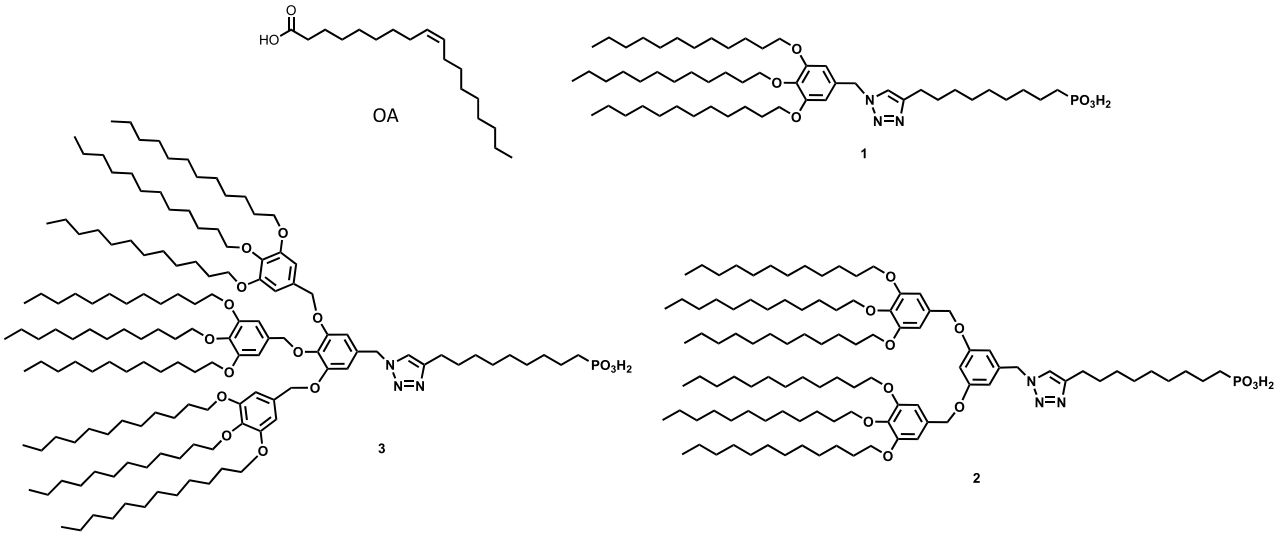

Figure 1. Structures of dendrimer ligands 1, 2, and 3 and oleic acid (OA) used in this study.

shells.[24] Self-assembly into larger superlattices is then influenced by such anisotropic coronas, resulting in various symmetry-breaking morphologies that have not been previously observed.[23,25]

A variety of plate assemblies due to ligand or organic surfactant effects have been observed in previous studies for 3D micron-sized superstructures;[26,27] however, investigations of thin films have largely focused on 2D assemblies in monolayer films.[28] In this work, we investigate ligand effects on anisotropic NC assembly through the use of dendrimer ligands of varying generation and cone angle in combination with rhombic plate NCs. The resulting films were analyzed with transmission electron microscopy (TEM) and grazing-incidence small- and wide-angle X-ray scattering (GISAXS and GIWAXS) to further describe their structure. Multilayered self-assembled films exhibit a distinct, highly controlled, offset architecture between layers of NCs, where the amount of offset increases with increased steric bulk of the ligand grafted on the surface of the NCs. Monte Carlo (MC) and molecular dynamics (MD) studies were conducted to elucidate the formation of these structures, explicitly accounting for nonuniform grafting densities on the anisotropic NCs. The results of these simulations show that ligand structure and steric interactions are both important considerations for NC film design, particularly for anisotropic NCs, as we aim to further understand these principles to effectively employ rational engineering of choice systems.

RESULTS AND DISCUSSION

Component Design. A series of ligands were designed and synthesized to study how different generation and cone angle of dendrimer ligands affect NC self-assembly. The complete series is shown in Figure 1, where two different generations, as well as different cone angle, or steric bulk, within the same generation are highlighted. This series allows for a direct comparison of the effects of these ligands on NC self-assembly processes. The specific ligand architecture used in this study was selected based on excellent control of NC assemblies previously studied, where interparticle spacing could be controlled effectively based on dendrimer generation.[29] Additionally, the larger generation dendrimer provided sufficient steric bulk to overcome NC−NC attractive forces to maintain interparticle spacing across various spherical particle sizes.[19,29] Given the structure of dendrimer ligands, they can provide surface protection of spherical particles, as they can pack effectively around a curved surface due to their cone angle.[30] These previous findings lead to questions of how ligands of these geometries bind to the surfaces of anisotropic NCs, and if their distinct geometries can lead to distinct or precisely controlled NC assemblies.

Complete synthetic details for the series of ligands used in this study are described in the Supporting Information. Briefly, using a similar synthetic strategy as was previously utilized due to its synthetic tunability,[29] targeted molecules **2a** and **3a** were obtained by reacting 5-(chloromethyl)-1,2,3-tris(dodecyloxy)-benzene with 3,5-dihydroxybenzoate or methyl 3,4,5-trihydroxybenzoate, respectively, using Williamson etherification. The subsequent esters were reduced with $LiAlH_4$, chlorinated, and then reacted with NaN_3 to obtain valuable intermediates **2d** and **3d**. To attach the selected surface binding group, phosphonic acid, which is known to bind to rare-earth-based NCs,[31] "click" chemistry was used to isolate final ligands **1**, **2**, and **3**.[32]

Separately, NCs of GdF_3:Yb/Er (20/2 mol %) were synthesized using previously reported methods.[3,31,33] These NCs are rhombic plates that have dimensions of 16.6 and 19.8 nm on their short and long sides, respectively, with a thickness of 3 nm, and have oleic acid (OA) on their surfaces after synthesis. Subsequently, the NCs were functionalized with each of the various dendrimers using a ligand exchange procedure[34] where the structure of the inorganic NCs is unchanged. Previous studies have used NMR to confirm the successful ligand exchange procedure;[29] however, the paramagnetic nature of the NCs in this study limits the characterization techniques. Successful ligand exchange was confirmed by thermogravimetric analysis,[31] shown in Figure S1, where NCs functionalized with OA show the organic decomposition at 190 °C, whereas the dendrimer ligands all decompose above 300 °C. This is additionally confirmed by observation of increased interparticle spacing of NC assemblies, which will be discussed in detail in the following discussion.

Interfacial Assembly. These dendrimer−NC hybrid materials (denoted ligand@NC) were then assembled using

DOI: 10.1021/acsnano.9b07348
ACS Nano 2019, 13, 14241−14251

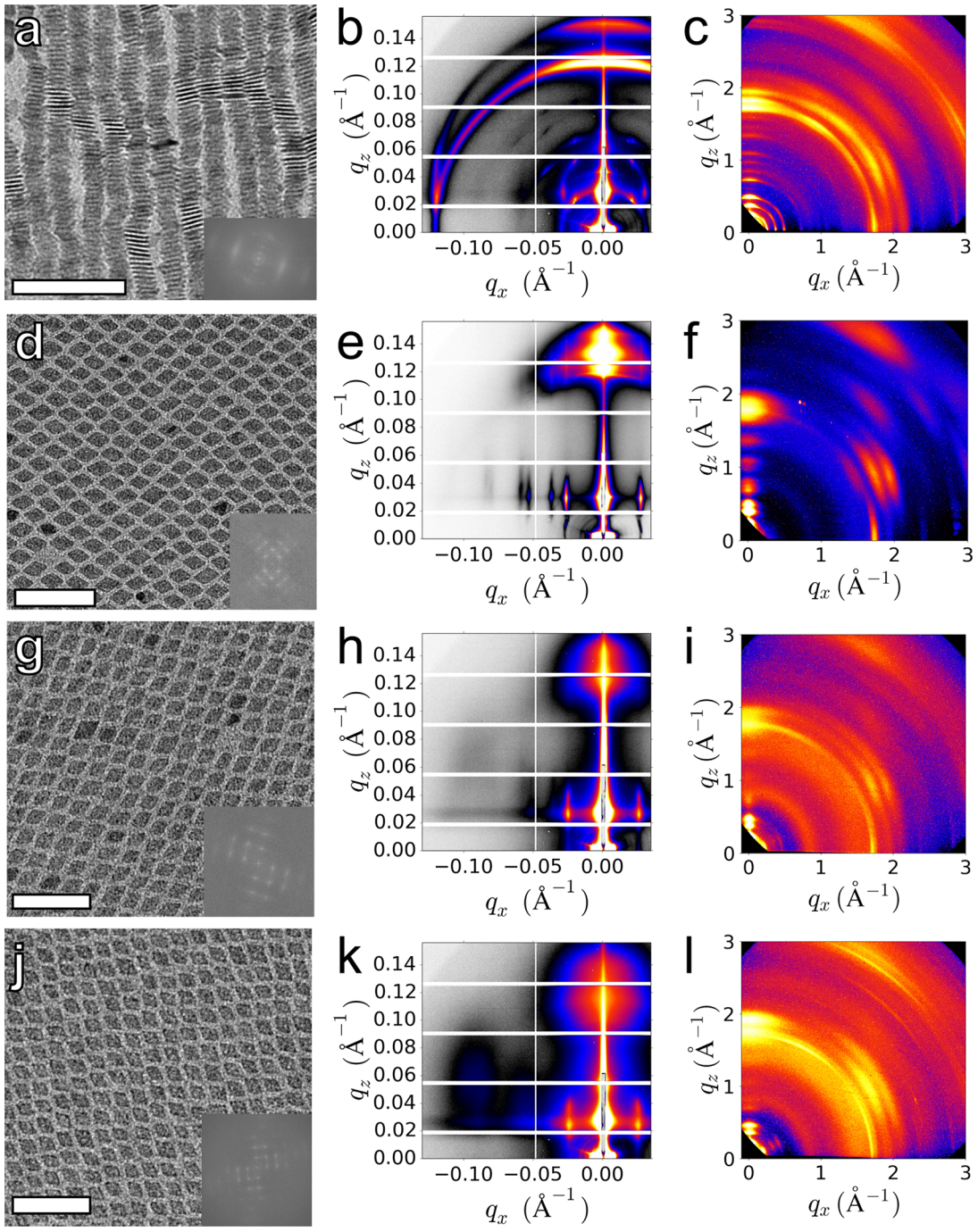

Figure 2. (a) TEM image of self-assembled OA@NC with calculated fast Fourier transform inset. (b) GISAXS and (c) GIWAXS of the same film. (d) TEM, (e) GISAXS, and (f) GIWAXS of self-assembled 1@NC. (g) TEM, (h) GISAXS, and (i) GIWAXS of self-assembled 2@NC. (j) TEM, (k) GISAXS, and (l) GIWAXS of self-assembled 3@NC. Scale bars are 100 nm.

a liquid−air interface method,[35] where subphases of varying polarity were investigated, as the Murray group has previously shown that the subphase of the assembly can tune the NC orientation, parallel or perpendicular, relative to the surface.[12] For the case of OA@NC, on commonly employed diethylene glycol, the NCs assemble into a mixture of columnar and lamellar grains, which corresponds to the NCs aligned either parallel (face-on) or perpendicular (edge-on) to the surface, respectively; however, the lamellar structure is the dominant film orientation, as shown in Figure 2a. This confirms previous findings, where a less polar subphase, such as tri- or tetraethylene glycol, favors the columnar structure and a more polar subphase directs the NCs toward a lamellar liquid-crystalline structure. The lamellar orientation was attributed in part due to the hydrophobicity of OA, as this would create repulsive interactions between the ligands and polar subphase.

Interestingly, for each dendrimer ligand, the dendrimer−NCs only align parallel to the subphase for each subphase investigated, shown in Figure 2d,g,j and Figure S2. In all cases, the same assembly architecture is observed. Four subphases of varying polarity were selected: ethylene glycol, diethylene glycol, triethylene glycol, and tetraethylene glycol. Due to the hydrophobicity of the ligands studied, it was hypothesized that an extension of previous results would be observed, as there

DOI: 10.1021/acsnano.9b07348
ACS Nano 2019, 13, 14241−14251

should be an increase in the repulsive interactions between the ligands and a polar subphase. However, this change in monolayer orientation suggests that there must be additional factors during the self-assembly process that have a strong influence on the final film morphology. Thus, further characterization of this film morphology was conducted to fully assess the films.

The addition of the dendrimer ligands also allows for monolayer films to be achieved, a challenge that was not easily accomplished in previous studies, as these NCs form multilayer films rapidly due to their interparticle attractive forces.[12] Successful monolayer assemblies exhibit the same film architecture, with only changes in the interparticle spacing. The interparticle spacing measured for **1**@NC from TEM images is 5.39 ± 0.71 nm, whereas it increases to 6.28 ± 1.17 and 6.89 ± 0.87 nm for NCs with larger ligands **2** and **3**, respectively.

These films were characterized using GISAXS and GIWAXS, allowing for a complete investigation of centimeter length-scale films transferred onto silicon wafers, confirming film uniformity, as well as the interparticle spacing and particle orientation in the films. The 2D GISAXS images are shown in Figure 2, highlighting the difference between panel b (OA@NC) and panels e, h, and k (**1**@NC, **2**@NC, and **3**@NC). The peak positions from these GISAXS patterns show the differences in NC alignments and are further confirmed qualitatively from the GIWAXS data. Films formed on each of the subphases were analyzed with GISAXS, shown in Figure S3. As can be seen from Figure S3, there are no significant differences between the films that were assembled on subphases of varying polarity, as no differences in film morphology were observed.

Line cuts along the in-plane direction, q_r, are shown in Figure 3, where fitting the primary peak was used to determine

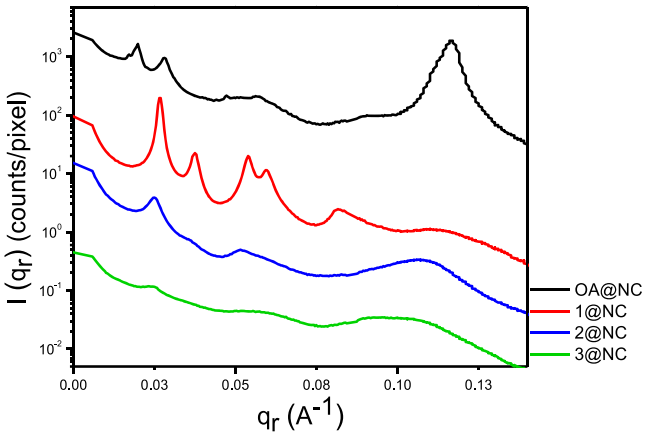

Figure 3. Line cuts for q_r values from 2D GISAXS patterns shown in Figure 2.

the repeat-spacing value for each lattice. For the case of OA@NC, the value from the primary peak of the line cut in this direction provides the stacking distance in the *z*-direction, as the plates are edge-on to the substrate. As **1**@NC, **2**@NC, and **3**@NC are all face-on to the substrate, fitting the primary peak in these cases provides the plate-to-plate distance in the *xy* plane, which are 4.7, 5.2, and 5.7 nm, respectively, in good agreement with the measured distance from TEM.

Vertical line cuts, q_z, of the GISAXS data are shown in Figure S4, where the NC stacking distance for multilayered films was extracted by fitting the peak near 0.12 $Å^{-1}$. The lamellar lattice of OA@NC has a vertical plate−plate stacking distance of 2.3 nm, and the dendrimer−NC samples have vertical stacking distances of 1.7, 2.2, and 2.7 nm for **1**@NC, **2**@NC, and **3**@NC, respectively. Based on the size of the ligands and the in-plane interparticle spacing measured from TEM and GISAXS, a larger plate−plate stacking distance was expected, particularly when compared to that of OA.

Figure S5 shows the angular curves extracted from the GISAXS data in Figure 2, where the full width at half-maxima estimate the average orientational tilt of the NCs relative to the substrate. For the dendrimer−NCs, values of 10.0, 11.9, and 17.9° were measured for **1**@NC, **2**@NC, and **3**@NC, respectively, whereas OA@NC has a measured tilt of 31.1° away from the substrate. The higher value for **3**@NC is attributed to areas of three or more NC layers thick within the film, where NCs that are perpendicular to their surrounding NCs can be found, as shown in Figure S7. For this larger ligand, the overall dendrimer−NC may be "softer"; that is, it has an increase of deformability of the organic ligand shell,[36,37] allowing for an increase in tolerance of mismatched alignment within the film,[19] as fewer of these instances can be found for **2**@NC and are very rare for the case of **1**@NC.

For multilayer films, typically the NC−NC interactions dictate NC alignment into a columnar architecture when the NCs align face-on to the substrate;[12] however, when the dendrimer ligands are grafted onto the surfaces of the NCs, a distinct architecture is observed. For each layer of the assembly, the particles are directionally offset, as highlighted in Figure 4, and this architecture can be achieved over large length scales, as shown in Figure S6. These films were characterized with TEM tilt tomography, as shown in Figure 4 and Figures S7 and S8, where an offset of 18.4 ± 2.4, 19.1 ± 3.0, and 23.3 ± 3.2% relative to the NC side lengths were observed for **1**@NC, **2**@NC, and **3**@NC, respectively. This offset is calculated as the distance between the edges of the two plates in the bilayer, highlighted in Figure 4, and converted to a percentage compared to the slide length of the NC. The observed architecture is most likely due to the large dendrimer ligands that were employed, as additional NC "softness" has been shown to lead to a variety of moiré patterns and binary superlattices in NC thin films.[29,38] With an increased "softness", the NC−NC interactions are diminished, making these differences in morphology of multilayer films achievable. However, no other 3D morphologies were observed, that is, changes in the architecture in the *z*-direction, as each layer of NCs was observed to be directionally offset from the previous layer. The only exception to this is shown in Figure S7, where, for the case of **3**@NC, if the films are more than three layers thick, NCs that are perpendicular to the substrate, stabilized by surrounding NCs, can be observed. If NC "softness" is the dominant driving force of this morphology, it is expected that additional 3D geometries would be observed, such as a rotation between NC layers, as previous studies have shown a large variety of moiré patterns present in similar NC systems.[29] This is due to an increase in the organic component in the overall NC material, or the "softness", which causes slipping between NC layers. Due to the high level of control of 3D assembly while employing such large ligands on the NCs, further investigation of how the ligands so effectively direct assembly was conducted.

Monte Carlo and Molecular Dynamics Simulations of Hybrid Systems. To elucidate the role of the ligands in the

DOI: 10.1021/acsnano.9b07348
ACS Nano 2019, 13, 14241−14251

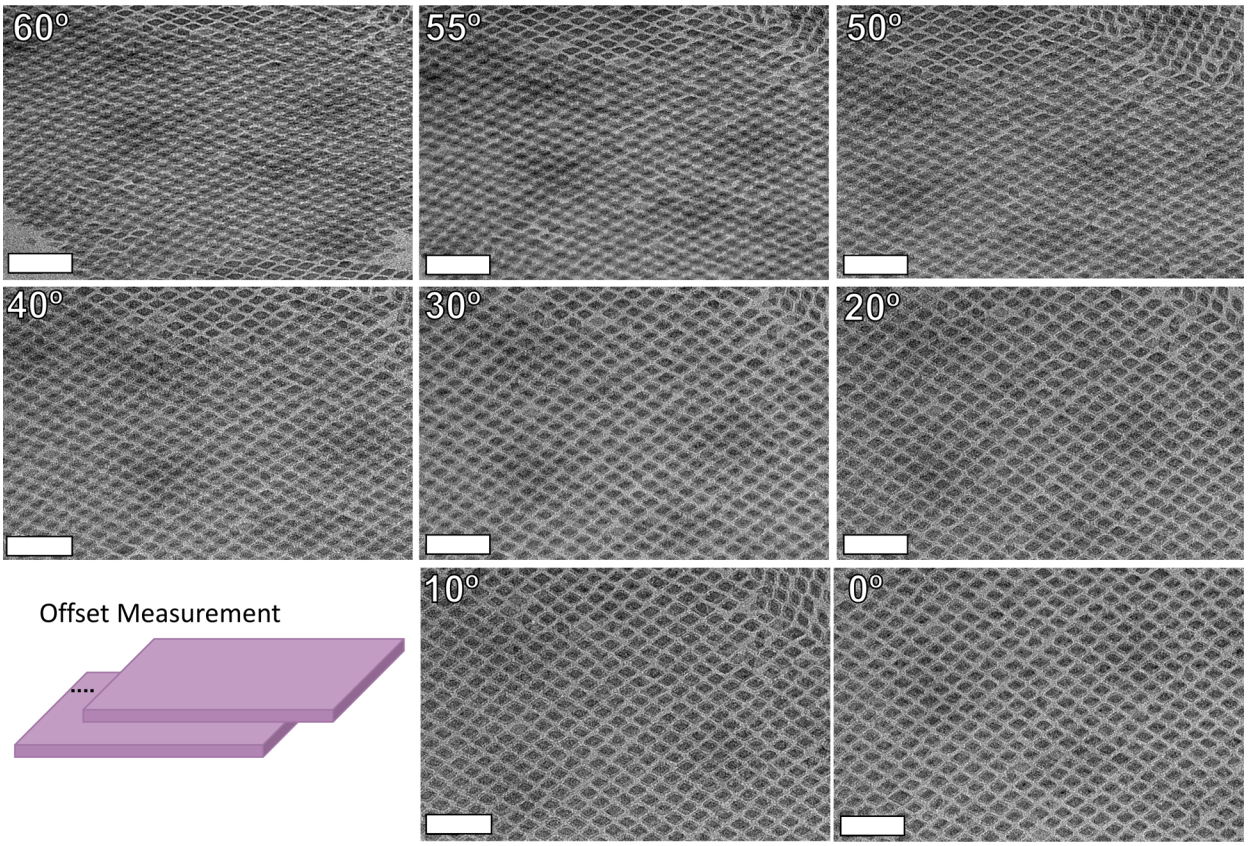

Figure 4. TEM tilt tomography of bilayer self-assembled 2@NC. Degree of tilt axis from the *x*-axis is provided in the top left, and a cartoon representing how the offset measurements were taken. Scale bars are 50 nm.

formation of this set of films and provide insights for future ligand and NC design, a series of simulations and theoretical predictions were performed. Previous studies involving the distribution of ligands on anisotropic particles have shown a natural partitioning of ligands to surface locations of increased curvature.[23,24,39,40] This partitioning can be understood as follows: for moderate to high grafting densities, local crowding drives each ligand to extend to its fully stretched configuration. The effect of crowding is expected to be uniformly distributed for an isotropic core but not for an anisotropic core. At positions of high curvature on anisotropic particles, ligands can occupy a larger volume going radially outward while retaining the same solid angle. The increase in accessible volume reduces the degree of crowding felt by the ligand from its neighbors, allowing it to relax toward an equilibrium configuration. This gain in both rotational and translational entropy associated with ligand conformation exceeds the loss in configurational entropy due to ligand partitioning and results in an anisotropic surface distribution. To the best of our knowledge, theories developed to capture such transitions have focused on linear ligand architecture.[23,40] A similar trend was demonstrated for models of simple ligands with large head groups,[24] but for branching motifs, the degree to which ligand partitioning will be affected is unknown.

To provide insight into any additional forces that might emerge due to the branched ligand architecture and to quantify the degree of partitioning, we developed a scaling theory that explicitly accounts for the effect of nonlinear grafts through a combination of both star polymer and branching scaling theories (see the Supporting Information).[23,41−46] Our main result defines a ligand end-to-end distance that scales as $R \sim r_o \sigma^{1/5} \nu^{1/5} b^{2/5} \left[\frac{N}{\Omega}\frac{b}{r_o}\right]^{3/5} \left[\frac{r_o \sigma^{1/2}}{N \Lambda \Omega^{3/2}}\right]^{1/10}$, where r_o is the size of the in-sphere radius of the anisotropic core, σ is the core grafting density, b is the statistical segment length of the ligand, ν is the excluded volume of the ligand, N is the degree of polymerization, and Λ is the effective degree of ligand nonlinearity. The parameter Ω is a shape term that defines both the shape of the grafting core and specific position on the particle surface. R can then be used to define the free energy of a ligand at various positions on the particle surface as $\beta F \sim \frac{R^2}{N^{7/16}\Lambda^{-1/16}} + \nu \frac{N^2 \sigma r_o^2}{(\Omega R)^3}$. The probability of finding a ligand at different surface position is simply $P \sim e^{-\beta F}$. Figure 5a plots the predicted partitioning probability, P, projected onto the respective surface positions on the nanoplate for ligands of increasing nonlinearity. Here, coloring is scaled such that the location of lowest partitioning probability is set to 0 and the highest is normalized to 1. In the limit of a linear ligand (no branching), we predict a slight partitioning away from the center of the larger facets (top and bottom faces) and a near isotropic distribution about the smaller faces (along edges) of the NC. Increasing ligand nonlinearity augments the preference for the smaller faces but also produces a secondary partitioning toward the vertices associated with the longer diagonal of the NC. Comparison of linear to branched scaling behavior reveals that the observed secondary effect arises due to an increase in the effective size of the ligand's statistical segment length that can be directly quantified as $b_{nl} \sim b_l \left(\frac{\sigma^{1/2} r_o}{N \Lambda}\right)^{1/4}$, where b_{nl} is the effective size of the

DOI: 10.1021/acsnano.9b07348
ACS Nano 2019, 13, 14241−14251

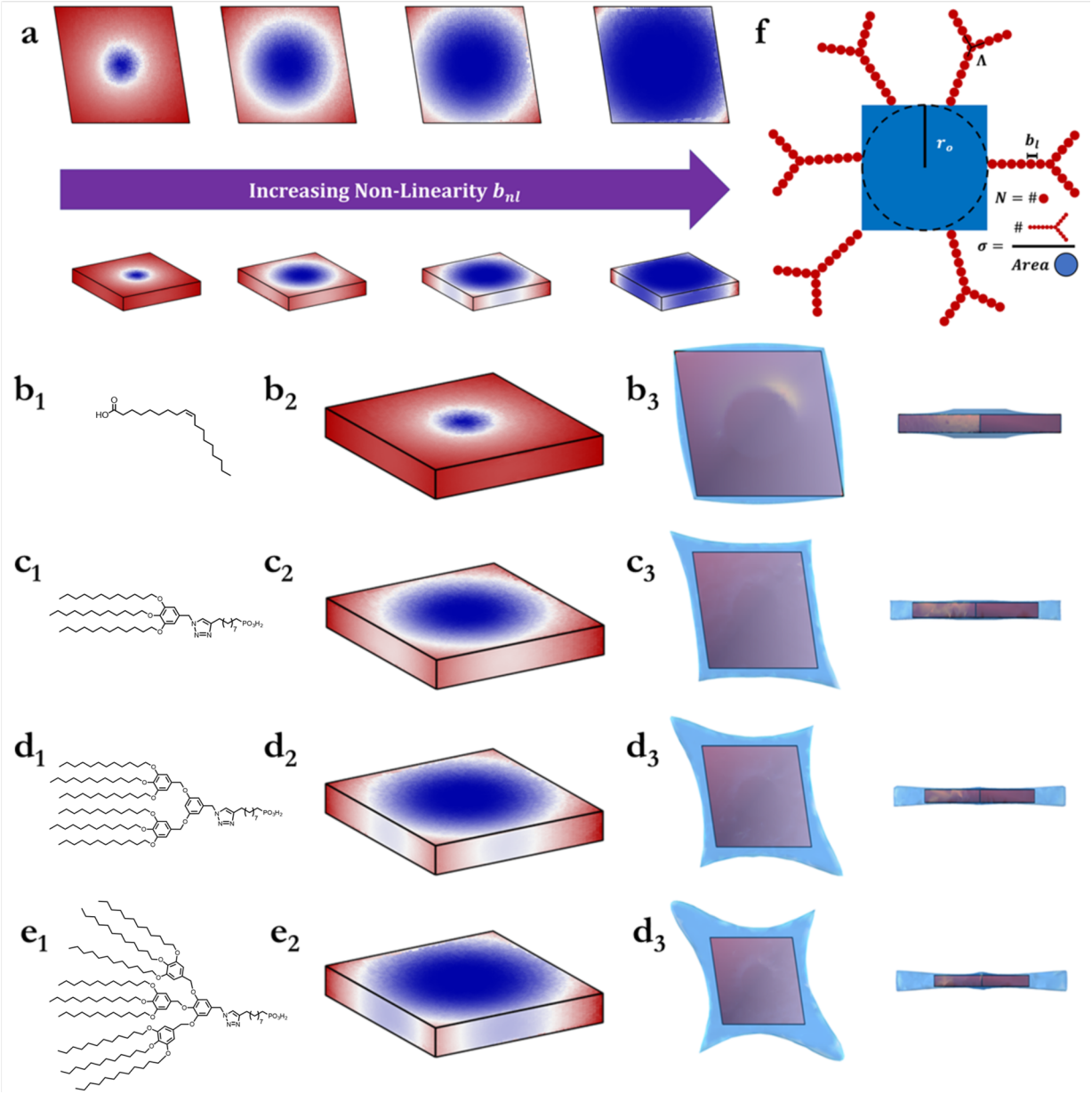

Figure 5. Scaling predictions for different ligand architectures. (a) Predicted ligand partitioning as a function of nonlinearity parameter b_{nl}. Colors indicate grafting probabilities (scaled between 0 and 1) at various locations on the rhombus surface. Top row shows a top-down view. Bottom row shows a side view. (b−e) Predictions for the specific ligand synthesized experimentally. Subscript 1 shows the ligand; subscript 2 shows the partition probability for the given ligand; subscript 3 shows the effective ligand corona about the rhombus. (f) Cartoon describing definitions of parameters employed. We observe more ligand partitioning as b_{nl} increases. The effective corona about the rhombus also transitions from conformal to concave, which then dictates the self-assembled morphology.

nonlinear ligand and b_l is the size of the linear ligand. A schematic further clarifying the definitions of the above parameters are shown in Figure 5f. These results suggest that we can employ branching ligand architecture as an additional handle to fine-tune the surface partitioning of ligands and possess a systematic, theoretical approach to estimate the effective increase in statistical segment size of nonlinear, grafted ligands relative to their linear counterparts.

The predicted probability, P, is then used to compute the average corona about the core. Briefly, the core is approximated as a series of surface mesh points that are roughly equidistant from each other. Each surface point has a ligand attachment probability P. A metropolis algorithm was then employed to place chains onto the particle surface, weighted by the probability. The number of chains grafted are set by the grafting density. The effective corona is then computed from averaging over 1×10^6 MC simulated coronas. Figure 5c−e shows the predicted partitioning and ligand coronas for the experimentally synthesized ligands scaled relative to a linear ligand (Figure 5b). As expected, we observe an increase in the grafting probability with increasing ligand nonlinearity (Figure 5b_2−e_2), which in turn tunes the effective corona morphology about the nanoplates (Figure 5b_3−e_3).[47] Here, we show a top-down view on the left and a side view on the right. We note here that the coronas around the NC become increasingly nonconformal with increasing ligand branching. Additionally, the corona morphology near the vertices grows larger in the z-direction, producing an additional

DOI: 10.1021/acsnano.9b07348
ACS Nano 2019, 13, 14241−14251

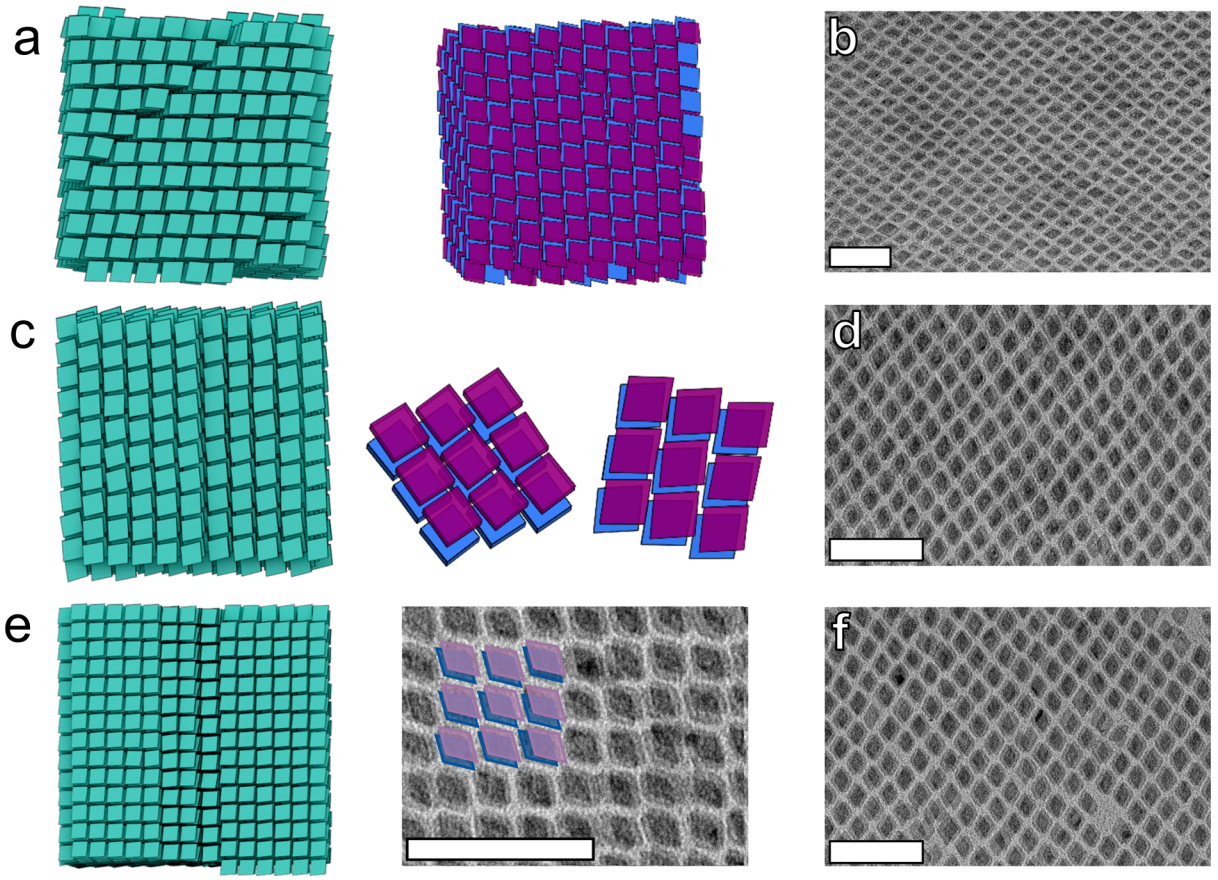

Figure 6. Comparison between simulation and experimental TEM images for multilayer assemblies: (a,b) 1@NC; (c,d) 2@NC; and (e,f) 3@NC. Analysis of the offset from simulation produces values of 16.3, 18.6, and 20.2 ± 2.0% as branching increases, in good agreement with experimental values of 18.4 ± 2.4, 19.1 ± 3.0, and 23.3 ± 3.2%. Additional images from simulations at various view points and microscopy with false coloring are provided to highlight NC offsets between layers. Scale bars are 100 nm.

concavity in the top and bottoms faces of the NC. These nonconformal coronas highlight the nontrivial interactions between rhombus-shaped NCs that dictate the final self-assembled morphology.

We performed MD simulations of the ligand-grafted NCs across a wide range of ligand nonlinearity b_{nl} using the HOOMD-Blue simulation engine.[48] The predicted coronas (Figure 5b$_3$–e$_3$) indicate the likelihood of finding a ligand at a given surface position and are directly related to how that specific location interacts with another surface position on a neighboring particle. Thus, we can create a rigid body of smaller surface beads that sit on the NC surface and attribute interaction strengths to each bead based on the grafting probability at their respective positions. To reduce the complexity of the simulation model, we categorize the continuous probability distribution into three distinct groups based on the value, p, of the scaled grafting probabilities: type A for $p \in [0,0.33)$, type B for $p \in [0.33,0.5)$, and type C for $p \in [0.5,1]$. Interactions between each bead type are Lennard-Jones (LJ) with ε and cutoffs computed from our scaling theory (see the Supporting Information for full details). Simulations were then initialized with 2744 NCs isotropically distributed. Each NC contains roughly 100 beads making up the rigid body, giving a total of 274 400 particles in each simulation. A driving force was applied to each particle to push them to a wall (mimicking the liquid–air interface) placed at the top of the simulation box. The wall also has an LJ-type attraction with the beads making up the NC, again with ε computed from our scaling theory. Simulations were run in an NVT ensemble at $T^* = 0.5$. The driving force was turned off after 1 M time steps, at which time there are enough NCs at the interface to nucleate crystallization. The system was then allowed to further equilibrate for 5 M time steps, followed by a production run of 10 M time steps. The left panels of Figure 6 show the final simulation snapshots for systems ran at the b_{nl} parameters corresponding to the synthesized ligands, and additional viewpoints from these simulations are also provided in Figure 6. Comparison with experimental TEM images (Figure 6b,d,f, right panels) shows nice agreement between simulation and experimental results. For the nonlinear ligands, there is an experimentally observed offset between subsequent layers of the NCs below the liquid–air interface that is not present in the linear ligands. The amount of offset (scaled relative to the NC side length) observed in the experimental images is 18.4 ± 2.4, 19.1 ± 3.0, and 23.3 ± 3.2% as compared with the values computed from our simulations of 16.3 ± 2.0, 18.6 ± 2.0, and 20.2 ± 2.0%.

To better explain the selective transitions between offset *versus* lamella stacking morphologies seen in both simulations and experiments, we utilize a Wertheim-like, first-order perturbation theory to predict the free energy of the NCs in both configurations, analogous to applications of Wertheim theory proposed by Lu *et al.* for DNA-mediated self-assembly.[23,49−52] Briefly, the theory calculates the change in the energy of formation for particles arranged on a lattice upon transitioning from a repulsive, "hard-particle" reference state to

DOI: 10.1021/acsnano.9b07348
ACS Nano 2019, 13, 14241−14251

one where a given surface distribution of interaction sites gives rise to a net attraction. To properly capture the physics governing our NC system, we expand the range of solid angles available to each surface site to interact with other particles in order to better model the more isotropic ligand−ligand interaction, as opposed to directed, hybridization driven interactions in DNA. Figure 7a plots the measured offset

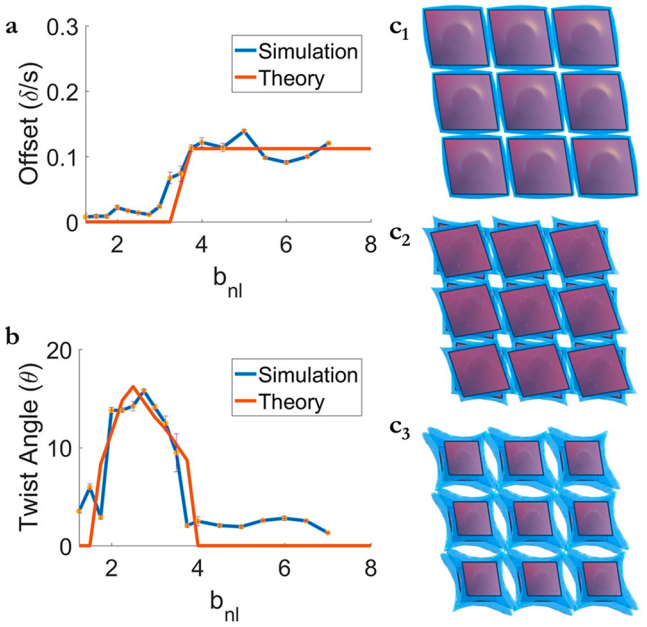

Figure 7. Theoretical predictions for lattice self-assembly. (a) Offset prediction as a function of ligand nonlinearity b_{nl} compared *versus* measured values from simulation. δ is the offset value, and s is the side length of the rhombus. (b) Prediction of relative twisting angle between layers as a function of ligand nonlinearity b_{nl} compared *versus* measured values from simulation. (c) Predicted lattice morphology for b_{nl} of 1 (c_1), 3 (c_2), and 5 (c_3) corresponding to a linear ligand, a nonlinear ligand before the offset transition, and a nonlinear ligand after the offset transition, respectively.

from simulations compared to theoretical predictions, revealing good agreement in the transition from a lamella to an offset motif at $b_{nl} \sim 3.5$. Figure 7c_{1-3} plots the predicted optimal sets of relative orientations and positions between the nanoplates using our theory at b_{nl} parameters of 1, 3, and 5, corresponding to a linear ligand, a nonlinear ligand before the transition, and a nonlinear ligand after the transition, respectively. For clarity, we visualize the NCs using their coronas to better represent how the shift in surface partitioning controls the observed morphologies.

Our results clearly indicate that the lamellae to offset transition is dictated by ligand crowding at the vertices with increasing graft nonlinearity (Figure 7a). For low crowding, particles can easily increase their net total ligand−ligand interactions with a slight twist relative to the layer above/below it. Twisting creates a lock-and-key interaction motif in-plane such that the vertex fits into the newly formed concave regions along the edge of the neighboring NCs while simultaneously creating additional vertex−vertex contacts with the layers above/below (Figure 7c_2). However, as crowding increases, this simple twist is not enough. Ligands partitioned toward vertices on the nanoplate are forced to extend by an additional amount as indicated by larger protrusions observed in the coronas, thus increasing their interaction range (Figure 5b_3−e_3). Concurrently, increased partitioning leads to a deficit of ligand concentration toward the center of the NCs, creating a concave motif for the top and bottom faces (Figure 5b_3−e_3). The increased extension leads to more favored vertex−vertex interactions in-plane, untwisting the NCs. However, the face−face contacts with the layers above and below the particles are no longer favored, as the corona is now concave. As a result, the system shifts layers upward along the *xy* direction relative to the previous layer. This shift increases ligand−ligand interactions by introducing additional vertex−vertex contacts *between* layers. Furthermore, shifting places vertices with high ligand concentration closer to the center of concave faces belonging to particles below it, creating another lock-and-key motif that maximizes out-of-plane ligand−ligand interactions, analogous to the driving force governing offsets observed in graphene layer-by-layer stacking (Figure 7c_3).[53] Direct quantification of the degree of twisting between layers further corroborates the idea of lock-and-key driven transition as we again observe a peak in the twist angle in both simulation and theory (Figure 7b).

CONCLUSIONS

Ligand design plays an important role in NC applications, as they can direct many of the resulting properties of the organic−inorganic hybrid materials, including self-assembly of NCs. This work highlighted how varying dendrimer ligand generation and steric interactions can be used to tune NC orientation as well as interparticle spacing and offset between layers of NCs in multilayer films. These films were characterized using GISAXS to confirm the film morphology, as well as TEM tilt tomography. MC and MD simulations with ligand probability distributions obtained from scaling theory were used to elucidate the ligand grafting distribution on the NCs, and perturbation theory was employed to characterize the driving forces governing self-assembly. As a result, we now possess a detailed molecular understanding of the how to control architectures found in multilayer films. These studies emphasized how ligand grafting distribution is an important consideration when designing systems for self-assembly, particularly for anisotropic NCs. For NC plates, large ligands create a corona around the NCs, which force an offset architecture in multilayer films due to a lock-and-key type of motif. In 2D films, this ligand corona leads to the corners and edges of the NC plates having more repulsive interactions between the more polar subphase used for assembly, resulting in the NC plates assembling parallel to the subphase surface. Our findings not only emphasize the idea that an anisotropic graft distribution plays a crucial role in controlling self-assembly but provide a systematic way to theoretically predict the resulting morphology purely from experimental design parameters such as core shape, grafting density, solvent condition, and ligand architecture. Such a model serves as a natural input into an inverse design framework that will enable us to *a priori* select for the best set of parameters to use in order to achieve a targeted self-assembled structure.[54]

METHODS

NMR. ^{1}H NMR (500 MHz) and ^{13}C NMR (126 MHz) spectra were recorded on a Bruker UNI500 NMR spectrometer. ^{1}H and ^{13}C chemical shifts (δ) are reported in parts per million (ppm), and coupling constants (J) are reported in hertz (Hz). The multiplicity of

DOI: 10.1021/acsnano.9b07348
ACS Nano 2019, 13, 14241−14251

signals in ^{1}H NMR spectra is described as "s" (singlet), "d" (doublet), "t" (triplet), "q" (quartet), "p" (pentet), "dd" (doublet of doublets), and "m" (multiplet). All spectra were referenced using solvent residual signals ($CDCl_3$: ^{1}H, δ 7.27 ppm; ^{13}C, δ 77.2 ppm).[55] Reaction progress was monitored by thin-layer chromatography using silica-gel-coated plates or ^{1}H NMR. Compounds were purified by filtration, precipitation, crystallization, or flash column chromatography using silica gel (Acros Organics, 90 Å, 35−70 μm) as indicated in corresponding procedures.

Mass Spectroscopy. Matrix-assisted laser desorption/ionization time-of-flight mass spectrometry (MALDI) was performed on a Bruker Ultraflex III mass spectrometer using dithranol as the matrix.

Electron Microscopy. TEM micrographs were collected using a JEOL 1400 microscope operated at 120 kV. The TEM was calibrated using a MAG*I*CAL TEM calibration standard.

Thermal Analysis. Thermogravimetric analysis was carried out using a TA Instruments TGA Q600 apparatus in the temperature range of 25 to 500 °C under N_2 flow at a heating rate of 10 °C/min.

Grazing-Incidence Small-Angle X-ray Scattering. Grazing-incidence small-angle X-ray scattering experiments were primarily performed at the Soft Matter Interfaces (SMI) 12-ID beamline of the National Synchrotron Light Source II at Brookhaven National Laboratory; some additional measurements were performed at the Complex Materials Scattering (CMS) 11-BM beamline. The X-ray energy was set to 16.1 keV (X-ray wavelength = 0.7701 Å) and microfocused (~20 μm horizontal by ~3 μm vertical) using a compound refractive lens system. X-ray scattering was collected using a three-detector setup, including a Dectris Pilatus 1 M (pixel size = 0.172 mm, distance = 3−8 m) for small-angle (SAXS) images, a Rayonix MX210 (pixel size 0.109 mm, distance 0.795 m) for medium-angle (MAXS), and a Dectris Pilatus 300 kW (pixel size 0.172 mm, distance 0.274 m) for wide-angle (WAXS). Detector data were converted to reciprocal space (q) by calibrating using known detector distances and confirmed using measurements of a standard sample (silver behenate). We define q_z to be the vertical (film normal) direction, q_x to be the orthogonal horizontal (in-plane) direction, q_y to be the direction along the beam, and $q_r = \sqrt{q_x^2 + q_y^2}$ to be the magnitude of the total in-plane scattering component. Samples were measured under vacuum using a typical exposure time of 10 s. GISAXS data were collected across a range of incident angles, both above and below the expected film-vacuum critical angle of the films (calculated to be approximately 0.18° at 16.1 keV, based on volumetric average of platelet and ligand scattering length densities).

Materials. All reagents were used without further purification unless specified. Methyl 3,4,5-trihydroxybenzoate (98%), methyl 3,5-dihydroxybenzoate (97%), 1-bromodecane (97%), NaN_3 (>99.5%), $LiAlH_4$ (95%), and oleic acid (OA, 90%, technical grade) were purchased from Aldrich. Thionyl chloride (>98%) was purchased from TCI. 10-Undeconoic phosphonic acid (<98%) was purchased from SiKemia Chemicals. Gadolinium oxide (Gd_2O_3, 99.9%), ytterbium oxide (Yb_2O_3, 99.9%), and erbium oxide (Er_2O_3, 99.9%) were purchased from GFS Chemicals and used without further purification. Lithium fluoride (LiF, 99.98%, extra pure, Acros Organics), trifluoroacetic acid ($C_2HF_3O_2$, 99.5%, for biochemistry, Acros Organics), 1-octadecene (ODE, 90%, technical grade, Acros Organics), potassium carbonate (reagent grade), sodium sulfate (anhydrous, reagent grade), silica gel (230−400 mesh, grade 60), dimethylfomamide, dichloromethane, chloroform, tetrahydrofuran, methanol, ethanol, hexanes, and ethyl acetate were purchased from Fisher Scientific and used without further purification. All solvents were ACS grade or higher.

Synthesis of GdF_3:Yb/Er (20/2 mol %). The procedure for creating the gadolinium trifluoroacetate [$Gd(CF_3COO)_3$], ytterbium trifluoroacetate [$Yb(CF_3COO)_3$], and erbium trifluoroacetate [$Er(CF_3COO)_3$] precursors is described elsewhere.[56] Briefly, for each precursor preparation, 10 g of the rare earth oxide was combined with 50 mL of deionized water and 50 mL of $C_2HF_3O_2$ in a round-bottom flask. The flask was submerged in a hot silicone bath, and the solution was magnetically stirred at 80 °C. Once the solution became clear, the solvents were evaporated using a rotary evaporator and the remaining precursor powder was collected. Note, the precursors are assumed to be in a hexahydrate form. The synthesis of the gadolinium trifluoride rhombic nanoplates doped with ytterbium and erbium [GdF_3:Yb/Er (20/2 mol %)] can also be found elsewhere[31] but, in short, were synthesized *via* rapid thermal decomposition of $Gd(CF_3COO)_3$, $Yb(CF_3COO)_3$, $Er(CF_3COO)_3$, and LiF. To form the nanocrystals, 30 mL of OA, 30 mL of ODE, 1.62 mmol of $Gd(CF_3COO)_3$, 8.33 mmol of LiF, 0.042 mmol of $Yb(CF_3COO)_3$, and 0.0042 mmol of $Er(CF_3COO)_3$ were added to a three-necked flask. While being stirred, the solution was heated to 125 °C and degassed for 3 h. After this vacuum step, the flask was purged with N_2 for 5 min and then ramped to (~20 °C/min) and maintained at the final reaction temperature of 290 °C, while still under N_2 flow. After 4 h, the reaction was terminated and the solution was cooled to room temperature. The particles were purified three times with a mixture of hexanes and ethanol and finally collected and stored in hexanes at a concentration of ~20 mg/mL.

Ligand Exchange with Dendrimers. A solution of 10 mg of dendrimeric ligands dissolved in 2 mL of chloroform was added to a 1 mL solution of 10 mg/mL oleylamine-capped NPs in hexanes, and the resulting mixture was stirred at 50 °C overnight. The reaction was quenched by addition of ethanol. The resulting precipitate was collected by centrifugation (6000 rpm, 5 min), and the supernatant liquid was discarded. The solid was redispersed in hexanes under ultrasonic irradiation (2 min) and precipitated by addition of methanol. This step was repeated at least twice to remove any excess ligands.

Self-Assembly of NCs. NC superlattices were obtained using the liquid−air interface assembly method described previously.[35] First, 1.7 mL of the selected subphase was loaded into a well (1.5 cm^2 × 1.0 cm deep machines into Teflon), and a suspension of NCs in hexanes (5 mg/mL) was cast onto the surface. This droplet was immediately covered with a glass slide, and the film was left to form over 12 h. The resulting film was transferred onto either TEM grids or Si/SiO_2 wafers by scooping or stamping the films onto the substrate. Any residual subphase was removed under vacuum before characterization.

Modeling of Ligand Corona and Lattice Energy Computation. Here, we adapt a scaling theory developed for grafting of linear ligands to an anisotropic core to account for nonlinear ligands. We define a chain swelling parameter, α, that explicitly accounts for chain branching—$\alpha^5 \sim N^{1/2}\nu[N\Lambda]^{-3/16}$, where N is chain length, ν is excluded volume, and Λ is the degree of branching. The derivation for the scaling theory using the new swelling parameter is analogous to that of linear chain (see derivation in the Supporting Information). Scaling analysis gives the free energy of ligand grafting at various positions on the particle surface that can then be used as a Boltzmann weight factor for the probability of chain grafting P. A metropolis algorithm was then employed to place chains onto the particle surface, weighted by P. The number of chains grafted are set by the grafting density. The effective corona is then computed from averaging over 1 × 10^6 MC simulated coronas. PMFs are then calculate between two particles with explicit coronas at various positions and relative orientations. The computed PMFs are then feed into the Wertheim-style lattice prediction approach proposed by Lu *et al.* to compute the excess free energy of lattice formation relative to a bare particle limit.[23,49−52]

Molecular Dynamics Simulation of Ligand-Grafted Particles. We first compute the partitioning probability of ligands on the surface of the nanoplate. This is performed *via* generating grid points on the particle surface and computing partitioning probability from our scaling theory. A set of potential mean forces was then computed between two grafted particles. While exact, creating a unique bead type for each point, the particle surface becomes prohibitively expensive for a molecular dynamics simulation (Figure S9a). To reduce the complexity, we categorize the continuous probability distribution into three distinct groups based on the value, P, of the scaled grafting probabilities: low for $P \in [0,0.33)$, medium for $P \in [0.33,0.5)$, and high for $P \in [0.5,1]$. NVT simulations are then performed at $T^* = 0.5$ for a system of 2744 NCs. Each NC contains

DOI: 10.1021/acsnano.9b07348
ACS Nano 2019, 13, 14241−14251

roughly 100 beads making up the rigid body, giving a total of 274 400 particles in each simulation. A driving force was applied to each particle to push them to a wall (mimicking the liquid−air interface) placed at the top of the simulation box. The wall also has an LJ-type interaction with the beads making up the NC. The driving force was turned off after 1 M time steps, at which time there are enough NCs at the interface to nucleate crystallization. The system was then allowed to further equilibrate for 5 M time steps, followed by a production run of 10 M time steps.

ASSOCIATED CONTENT

Supporting Information

The Supporting Information is available free of charge at https://pubs.acs.org/doi/10.1021/acsnano.9b07348.

Ligand synthesis procedures and characterization; additional microscopy; GISAXS data analysis; scaling theory for branching ligand architecture; mapping of scaling prediction to simulation (PDF)

AUTHOR INFORMATION

Corresponding Authors

*E-mail: sglotzer@umich.edu.
*E-mail: cbmurray@sas.upenn.edu.

ORCID

Katherine C. Elbert: 0000-0001-9019-1506
Nadia M. Krook: 0000-0003-3308-9040
Kevin G. Yager: 0000-0001-7745-2513
Russell J. Composto: 0000-0002-5906-2594

Author Contributions

#K.C.E. and T.V. contributed equally to this work.

Notes

The authors declare no competing financial interest.

ACKNOWLEDGMENTS

The authors acknowledge support from the Office of Naval Research Multidisciplinary University Research Initiative Award ONR N00014-18-1-2497. K.C.E. acknowledges support from the NSF Graduate Research Fellowship Program under Grant No. DGE-1321851. W.E.Z. was supported by a National Defense Science and Engineering Graduate (NDSEG) Fellowship, 32 CFR 168a, awarded by the Department of Defense, Air Force Office of Scientific Research under Contract No. FA9550-11-C-0028. This work used the Extreme Science and Engineering Discovery Environment (XSEDE), which is supported by National Science Foundation Grant ACI-1053575; XSEDE Award DMR 140129. Computational resources and services were also provided by Advanced Research Computing (ARC-TS) at the University of Michigan, Ann Arbor, MI. This research was supported by the National Science Foundation with support from the POLYMERS-DMR-1507713 and 1905912 (N.M.K., R.J.C.), PIRE-OISE-1545884 (N.M.K., C.B.M., R.J.C.), and MRSEC-DMR-1720530 (N.M.K., C.B.M., R.J.C.) programs. This research used resources of the Center for Functional Nanomaterials and the National Synchrotron Light Source II, which are U.S. DOE Office of Science Facilities, at Brookhaven National Laboratory under Contract No. DE-SC0012704. C.B.M. acknowledges the Richard Perry University Professorship at the University of Pennsylvania.

REFERENCES

(1) Shi, Q.; Si, K. J.; Sikdar, D.; Yap, L. W.; Premaratne, M.; Cheng, W. Two-Dimensional Bipyramid Plasmonic Nanoparticle Liquid Crystalline Superstructure with Four Distinct Orientational Packing Orders. *ACS Nano* **2016**, *10*, 967−976.

(2) Boles, M. A.; Engel, M.; Talapin, D. V. Self-Assembly of Colloidal Nanocrystals: From Intricate Structures to Functional Materials. *Chem. Rev.* **2016**, *116*, 11220−11289.

(3) Ye, X.; Collins, J. E.; Kang, Y.; Chen, J.; Chen, D. T. N.; Yodh, A. G.; Murray, C. B. Morphologically Controlled Synthesis of Colloidal Upconversion Nanophosphors and Their Shape-Directed Self-Assembly. *Proc. Natl. Acad. Sci. U. S. A.* **2010**, *107*, 22430−22435.

(4) Shevchenko, E. V.; Talapin, D. V.; Kotov, N. A.; O'Brien, S.; Murray, C. B. Structural Diversity in Binary Nanoparticle Superlattices. *Nature* **2006**, *439*, 55−59.

(5) Singh, G.; Chan, H.; Baskin, A.; Gelman, E.; Repnin, N.; Král, P.; Klajn, R. Self-Assembly of Magnetite Nanocubes into Helical Superstructures. *Science* **2014**, *345*, 1149−1153.

(6) Macfarlane, R. J.; Lee, B.; Jones, M. R.; Harris, N.; Schatz, G. C.; Mirkin, C. A. Nanoparticle Superlattice Engineering with DNA. *Science* **2011**, *334*, 204−208.

(7) van Anders, G.; Klotsa, D.; Ahmed, N. K.; Engel, M.; Glotzer, S. C. Understanding Shape Entropy through Local Dense Packing. *Proc. Natl. Acad. Sci. U. S. A.* **2014**, *111*, E4812−E4821.

(8) Disch, S.; Wetterskog, E.; Hermann, R. P.; Korolkov, D.; Busch, P.; Boesecke, P.; Lyon, O.; Vainio, U.; Salazar-Alvarez, G.; Bergström, L.; Bruckel, T. Structural Diversity in Iron Oxide Nanoparticle Assemblies as Directed by Particle Morphology and Orientation. *Nanoscale* **2013**, *5*, 3969−3975.

(9) Lu, F.; Yager, K. G.; Zhang, Y.; Xin, H.; Gang, O. Superlattices Assembled through Shape-Induced Directional Binding. *Nat. Commun.* **2015**, *6*, 6912.

(10) Li, R.; Bian, K.; Hanrath, T.; Bassett, W. A.; Wang, Z. Decoding the Superlattice and Interface Structure of Truncate PbS Nanocrystal-Assembled Supercrystal and Associated Interaction Forces. *J. Am. Chem. Soc.* **2014**, *136*, 12047−12055.

(11) Wang, Y.; Santos, P. J.; Kubiak, J. M.; Guo, X.; Lee, M. S.; Macfarlane, R. J. Multistimuli Responsive Nanocomposite Tectons for Pathway Dependent Self-Assembly and Acceleration of Covalent Bond Formation. *J. Am. Chem. Soc.* **2019**, *141*, 13234−13243.

(12) Paik, T.; Ko, D.-K.; Gordon, T. R.; Doan-Nguyen, V.; Murray, C. B. Studies of Liquid Crystalline Self-Assembly of GdF_3 Nanoplates by In-Plane, Out-of-Plane SAXS. *ACS Nano* **2011**, *5*, 8322−8330.

(13) Diroll, B. T.; Greybush, N. J.; Kagan, C. R.; Murray, C. B. Smectic Nanorod Superlattices Assembled on Liquid Subphases: Structure, Orientation, Defects, and Optical Polarization. *Chem. Mater.* **2015**, *27*, 2998−3008.

(14) Baker, J. L.; Widmer-Cooper, A.; Toney, M. F.; Geissler, P. L.; Alivisatos, A. P. Device-Scale Perpendicular Alignment of Colloidal Nanorods. *Nano Lett.* **2010**, *10*, 195−201.

(15) Yu, Y.; Yu, D.; Orme, C. A. Reversible, Tunable, Electric-Field Driven Assembly of Silver Nanocrystal Superlattices. *Nano Lett.* **2017**, *17*, 3862−3869.

(16) Singh, A.; English, N. J.; Ryan, K. M. Highly Ordered Nanorod Assemblies Extending over Device Scale Areas and in Controlled Multilayers by Electrophoretic Deposition. *J. Phys. Chem. B* **2013**, *117*, 1608−1615.

(17) Zhang, J.; Santos, P. J.; Gabrys, P. A.; Lee, S.; Liu, C.; Macfarlane, R. J. Self-Assembling Nanocomposite Tectons. *J. Am. Chem. Soc.* **2016**, *138*, 16228−16231.

(18) Boles, M. A.; Talapin, D. V. Self-Assembly of Tetrahedral CdSe Nanocrystals: Effective "Patchiness" *via* Anisotropic Steric Interaction. *J. Am. Chem. Soc.* **2014**, *136*, 5868−5871.

(19) Jishkariani, D.; Elbert, K. C.; Wu, Y.; Lee, J. D.; Hermes, M.; Wang, D.; Van Blaaderen, A.; Murray, C. B. Nanocrystal Core Size and Shape Substitutional Doping and Underlying Crystalline Order in Nanocrystal Superlattices. *ACS Nano* **2019**, *13*, 5712−5719.

(20) Ye, X.; Zhu, C.; Ercius, P.; Raja, S. N.; He, B.; Jones, M. R.; Hauwiller, M. R.; Liu, Y.; Xu, T.; Alivisatos, A. P. Structural Diversity

DOI: 10.1021/acsnano.9b07348
ACS Nano 2019, 13, 14241−14251

in Binary Superlattices Self-Assembled from Polymer-Grafted Nanocrystals. *Nat. Commun.* **2015**, *6*, 10052.
(21) Castelli, A.; de Graaf, J.; Marras, S.; Brescia, R.; Goldoni, L.; Manna, L.; Arciniegas, M. P. Understanding and Tailoring Ligand Interactions in the Self-Assembly of Branched Colloidal Nanocrystals into Planar Superlattices. *Nat. Commun.* **2018**, *9*, 1141.
(22) Antanovich, A.; Prudnikau, A.; Matsukovich, A.; Achtstein, A.; Artemyev, M. Self-Assembly of CdSe Nanoplatelets into Stacks of Controlled Size Induced by Ligand Exchange. *J. Phys. Chem. C* **2016**, *120*, 5764−5775.
(23) Lu, F.; Vo, T.; Zhang, Y.; Frenkel, A.; Yager, K. G.; Kumar, S.; Gang, O. Unusual Packing of Soft-Shelled Nanocubes. *Sci. Adv.* **2019**, *5*, eaaw2399.
(24) Santos, A.; Millan, J. A.; Glotzer, S. C. Facetted Patchy Particles through Entropy-Driven Patterning of Mixed Ligand SAMS. *Nanoscale* **2012**, *4*, 2640−2650.
(25) Ye, X.; Chen, J.; Engel, M.; Millan, J. A.; Li, W.; Qi, L.; Xing, G.; Collins, J. E.; Kagan, C. R.; Li, J.; Glotzer, S. C.; Murray, C. B. Competition of Shape and Interaction Patchiness for Self-Assembling Nanoplates. *Nat. Chem.* **2013**, *5*, 466.
(26) Zhou, W.; Yao, M.; Guo, L.; Li, Y.; Li, J.; Yang, S. Hydrazine-Linked Convergent Self-Assembly of Sophisticated Concave Polyhedrons of-Ni(OH) 2 and NiO from Nanoplate Building Blocks. *J. Am. Chem. Soc.* **2009**, *131*, 2959−2964.
(27) Wu, J.; Duan, F.; Zheng, Y.; Xie, Y. Synthesis of Bi 2 WO 6 Nanoplate-Built Hierarchical Nest-Like Structures with Visible-Light-Induced Photocatalytic Activity. *J. Phys. Chem. C* **2007**, *111*, 12866−12871.
(28) Ye, X.; Chen, J.; Eric Irrgang, M.; Engel, M.; Dong, A.; Glotzer, S. C.; Murray, C. B. Quasicrystalline Nanocrystal Superlattice with Partial Matching Rules. *Nat. Mater.* **2017**, *16*, 214−219.
(29) Elbert, K. C.; Jishkariani, D.; Wu, Y.; Lee, J. D.; Donnio, B.; Murray, C. B. Design, Self-Assembly, and Switchable Wettability in Hydrophobic, Hydrophilic, and Janus Dendritic Ligand−Gold Nanoparticle Hybrid Materials. *Chem. Mater.* **2017**, *29*, 8737−8746.
(30) Elbert, K. C.; Lee, J. D.; Wu, Y.; Murray, C. B. Improved Chemical and Colloidal Stability of Gold Nanoparticles through Dendron Capping. *Langmuir* **2018**, *34*, 13333−13338.
(31) Krook, N. M.; Ford, J.; Maréchal, M.; Rannou, P.; Meth, J. S.; Murray, C. B.; Composto, R. J. Alignment of Nanoplates in Lamellar Diblock Copolymer Domains and the Effect of Particle Volume Fraction on Phase Behavior. *ACS Macro Lett.* **2018**, *7*, 1400−1407.
(32) Iha, R. K.; Wooley, K. L.; Nyström, A. M.; Burke, D. J.; Kade, M. J.; Hawker, C. J. Applications of Orthogonal "Click" Chemistries in the Synthesis of Functional Soft Materials. *Chem. Rev.* **2009**, *109*, 5620−5686.
(33) Paik, T.; Chacko, A.-M.; Mikitsh, J. L.; Friedberg, J. S.; Pryma, D. A.; Murray, C. B. Shape-Controlled Synthesis of Isotopic Yttrium-90-Labeled Rare Earth Fluoride Nanocrystals for Multimodal Imaging. *ACS Nano* **2015**, *9*, 8718−8728.
(34) Dong, A.; Ye, X.; Chen, J.; Kang, Y.; Gordon, T.; Kikkawa, J. M.; Murray, C. B. A Generalized Ligand-Exchange Strategy Enabling Sequential Surface Functionalization of Colloidal Nanocrystals. *J. Am. Chem. Soc.* **2011**, *133*, 998−1006.
(35) Dong, A.; Chen, J.; Vora, P. M.; Kikkawa, J. M.; Murray, C. B. Binary Nanocrystal Superlattice Membranes Self-Assembled at the Liquid−Air Interface. *Nature* **2010**, *466*, 474−477.
(36) Diroll, B. T.; Weigandt, K. M.; Jishkariani, D.; Cargnello, M.; Murphy, R. J.; Hough, L. A.; Murray, C. B.; Donnio, B. Quantifying "Softness" of Organic Coatings on Gold Nanoparticles Using Correlated Small-Angle X-Ray and Neutron Scattering. *Nano Lett.* **2015**, *15*, 8008−8012.
(37) Tan, R.; Zhu, H.; Cao, C.; Chen, O. Multi-Component Superstructures Self-Assembled from Nanocrystal Building Blocks. *Nanoscale* **2016**, *8*, 9944−9961.
(38) Coropceanu, I.; Boles, M. A.; Talapin, D. V. Systematic Mapping of Binary Nanocrystal Superlattices: The Role of Topology in Phase Selection. *J. Am. Chem. Soc.* **2019**, *141*, 5728−5740.
(39) O'Brien, M. N.; Girard, M.; Lin, H.-X.; Millan, J. A.; Olvera de la Cruz, M.; Lee, B.; Mirkin, C. A. Exploring the Zone of Anisotropy and Broken Symmetries in DNA-Mediated Nanoparticle Crystallization. *Proc. Natl. Acad. Sci. U. S. A.* **2016**, *113*, 10485−10490.
(40) Galati, E.; Tebbe, M.; Querejeta-Fernández, A.; Xin, H. L.; Gang, O.; Zhulina, E. B.; Kumacheva, E. Shape-Specific Patterning of Polymer-Functionalized Nanoparticles. *ACS Nano* **2017**, *11*, 4995−5002.
(41) Daoud, M.; Cotton, J. P. Star Shaped Polymers : A Model for the Conformation and Its Concentration Dependence. *J. Phys. (Paris)* **1982**, *43*, 531−538.
(42) Daoud, M.; Joanny, J. F. Conformation of Branched Polymers. *J. Phys. (Paris)* **1981**, *42*, 1359−1371.
(43) Zimm, B. H.; Stockmayer, W. H. The Dimensions of Chain Molecules Containing Branches and Rings. *J. Chem. Phys.* **1949**, *17*, 1301−1314.
(44) Dobson, G. R.; Gordon, M. Configurational Statistics of Highly Branched Polymer Systems. *J. Chem. Phys.* **1964**, *41*, 2389−2398.
(45) Flory, P. J. *Principles of Polymer Chemistry*, 1st ed.; Cornell University Press: Ithaca, NY, 1953.
(46) De Gennes, P. G. *Scaling Concepts in Polymer Physics*, 1st ed.; Cornell University Press: Ithaca, NY, 1979.
(47) Anderson, J. A.; Eric Irrgang, M.; Glotzer, S. C. Scalable Metropolis Monte Carlo for Simulation of Hard Shapes. *Comput. Phys. Commun.* **2016**, *204*, 21−30.
(48) Glaser, J.; Nguyen, T. D.; Anderson, J. A.; Lui, P.; Spiga, F.; Millan, J. A.; Morse, D. C.; Glotzer, S. C. Strong Scaling of General-Purpose Molecular Dynamics Simulations on GPUs. *Comput. Phys. Commun.* **2015**, *192*, 97−107.
(49) Wertheim, M. S. Fluids with Highly Directional Attractive Forces. I. Statistical Thermodynamics. *J. Stat. Phys.* **1984**, *35*, 19−34.
(50) Wertheim, M. S. Fluids with Highly Directional Attractive Forces. II. Thermodynamic Perturbation Theory and Integral Equations. *J. Stat. Phys.* **1984**, *35*, 35−47.
(51) Wertheim, M. S. Fluids with Highly Directional Attractive Forces. III. Multiple Attraction Sites. *J. Stat. Phys.* **1986**, *42*, 459−476.
(52) Wertheim, M. S. Fluids with Highly Directional Attractive Forces. IV. Equilibrium Polymerization. *J. Stat. Phys.* **1986**, *42*, 477−492.
(53) Shan, Y.; Li, Y.; Huang, D.; Tong, Q.; Yao, W.; Liu, W.-T.; Wu, S. Stacking Symmetry Governed Second Harmonic Generation in Graphene Trilayers. *Sci. Adv.* **2018**, *4*, eaat0074.
(54) Srinivasan, B.; Vo, T.; Zhang, Y.; Gang, O.; Kumar, S.; Venkatasubramanian, V. Designing DNA-Grafted Particles That Self-Assemble into Desired Crystalline Structures Using the Genetic Algorithm. *Proc. Natl. Acad. Sci. U. S. A.* **2013**, *110*, 18431−18435.
(55) Gottlieb, H. E.; Kotlyar, V.; Nudelman, A. NMR Chemical Shifts of Common Laboratory Solvents as Trace Impurities. *J. Org. Chem.* **1997**, *62*, 7512−7515.
(56) Najmr, S.; Jishkariani, D.; Elbert, K. C.; Donnio, B.; Murray, C. B. A Semi-Combinatorial Approach for Investigating Polycatenar Ligand-Controlled Synthesis of Rare-Earth Fluoride Nanocrystals. *Nanoscale* **2017**, *9*, 8107−8112.

DOI: 10.1021/acsnano.9b07348
ACS Nano 2019, 13, 14241−14251